Vacuum 171 (2020) 108993

Contents lists available at ScienceDirect

Vacuum

journal homepage: http://www.elsevier.com/locate/vacuum

Mechanisms of graphite crucible degradation in contact with Si–Al melts at high temperatures and vacuum conditions

Arman Hoseinpur [a,*], Jafar Safarian [a,b]

[a] Department of Materials Technology, Norwegian University of Science and Technology (NTNU), Trondheim, 7034, Norway
[b] Norwegian Center for Sustainable Solar Cell Technology, Norway

ARTICLE INFO

Keywords:
Passive layer
Silicon
Silicon carbide (SiC)
Aluminum carbide (Al_4C_3)
Melt infiltration
Vacuum
Vapor

ABSTRACT

Graphite is a common refractory material for processing high purity silicon; however, it cannot be applied for holding Si–Al melts at high temperatures due to significant melt infiltration into the crucible. This research investigates the interaction mechanisms of graphite with Si at 1500 and 1800 °C and graphite with Si-20 wt%Al melt at 1500 °C and vacuum conditions. Scanning Electron Microscopy (SEM) and X-Ray powder Diffraction (XRD) methods are applied to investigate the morphology and chemistry of the phases formed at the interface of graphite with Si and graphite with Si–Al melts. Results showed that Al in Si–Al melt infiltrates into graphite leading to the formation of aluminum carbides, which accompanies with volume expansion and therefore the crucible destruction. The formation mechanisms of silicon carbide (SiC) from Si melt, and aluminum carbide from a Si-20 wt%Al melt in graphite crucibles are compared. It is shown that graphite crucible can be passivated by controlled formation of a dense SiC layer on the surface, and further can be used for different melts treatments with no melt infiltration and crucible destruction. The effect of temperature on the growth of the passive SiC layer was also investigated.

1. Introduction

Silicon (Si) is an important material for solar power production and energy storage purposes. Application of Si would be on increase in future in the energy sector. According to the sky scenario developed by Shell® [1] it is anticipated that 37% of the world energy would be generated by solar cells in the year 2070. Currently more than 95% of the solar panels are produced of Si [2]. Metallurgical methods for production pure Si have been vastly researched in the past two decades since they are economic and more environmentally friendly. Elkem Solar®, Silicor®, and Ferroglobe® processes are the three metallurgical methods established for production solar grade silicon (SoG-Si). These methods apply a combination of pyrometallurgical methods to produce the SoG-Si including of slag refining [3], solvent refining [4], and vacuum refining [5]. In addition to the application of Si in solar panels, it is also being researched to be applied as the Phase Change Material (PCM) for storing energy in high temperature batteries [6], where Si is melted by absorbing the energy in the charging cycle and solidifies to release energy in the discharging cycle. Repetitive melting and solidifying of silicon in high temperature batteries makes it necessary to find an appropriate refractory material for the melt container.

Molten Si and its alloys are highly reactive to the point of being labeled "a universal solvent" [7]. Among the metal carbides (WC, TiC, ZrC, SiC and TaC), oxides (Al_2O_3), and nitrides (Si_3N_4) that are tested for holding Si melts, graphite has become the most applicable and well-known refractory material for treating Silicon (Si) melts especially in high temperatures and vacuum conditions [7–11]. This arises from the unique properties of graphite such as being relatively inert (small carbon solubility in silicon) in contact with Si melt, machinability, high temperature stability, and the ease of purifying it. Up to now, graphite has been widely used for holding Si and its alloys in molten state at high temperatures for metallurgical purposes. It has also been found as an appropriate container for thermal storage batteries to hold the PCM alloy Si–Fe–B [12]. This makes the Si melt interaction with graphite at high temperatures to be necessary to investigate. Literature studies [8, 13–15] show as the Si melt contacts with the graphite crucible a thin layer of SiC forms on the graphite. In addition, liquid Si infiltrates to the graphite crucible and a micrometric infiltrated layer consisting of SiC forms in the graphite body. Casado et al. [8]. investigated Si melt infiltration to various graphite materials and showed that melt

* Corresponding author.
E-mail address: arman.h.kermani@ntnu.no (A. Hoseinpur).
URL: https://www.susoltech.no (J. Safarian).

https://doi.org/10.1016/j.vacuum.2019.108993
Received 27 August 2019; Received in revised form 17 September 2019; Accepted 2 October 2019
Available online 5 October 2019

Table 1
Physical and chemical properties of the graphite crucible and samples investigated in this research.

Bulk density (Ton/m^3)	1.90
Hardness (HSD)	60
Electrical resistivity (μΩ.m)	9.5
Flexural strength (M.Pa)	54
Compressive strength (G.Pa)	103
Tensile strength (M.Pa)	29
Young's modulus (GPa)	11.8
Thermal conductivity W/(m.K)	140

infiltration has a relation with the crystallinity of the graphite and the melt infiltrates more to the amorphous graphite. Polkowski et al. [16]. investigated the Si–B interaction with graphite and SiC crucibles for thermal storage purposes. They showed when B is added to the Si melt, SiC layer forms on the graphite surface and after long times a thin layer of Boron carbide (B_4C) forms on the SiC layer.

Refining is an integrate step in production of SoG-Si, where the concentration of Phosphorus (P) must be less than 0.2 ppmM. Vacuum refining is the most effective method for removing volatile species such as P from Si. Vacuum refining is based on the difference in vapor pressure of the impurity and solvent. Safarian [17] investigated the evaporation of the metals in vacuum conditions and concluded the effective pressure for intensive evaporation of a metal is 0.2 of its standard pressure ($p^{\circ}_{eff} = 0.2\,p^{\circ}_{i}$). Considering the great difference in standard vapor pressures of Si and P at the melting point of Si ($p^{\circ}_{P} = 3.2 \times 10^{10}$ Pa, $p^{\circ}_{Si} = 0.79$ Pa) it can be concluded that vacuum refining would be an effective method for removal of P from Si. P removal from Si by means of vacuum refining has been investigated for more than 25 years [11,17–19]. However the authors reported the P removal from Si–Al alloy in Ref. [20] and showed alloying of Si with 20 wt% Al accelerated the kinetics of P removal from Si. In addition, it was shown that by alloying the Si, vacuum refining could be done at temperatures lower than melting point of Si. This makes the Si–Al system to be interesting for further investigations, however, this alloy shows intensive interactions with graphite crucibles. This problem must be addressed to make it possible to do further investigations on Si–Al alloys. The high temperature vacuum refining is a challenging process for most of the refractory materials that are appropriate for holding Si melts. Although Alumina (Al_2O_3) and Quartz (SiO_2) crucibles can be applied for holding Si melts but both of them decompose at high temperatures when they are under reduced pressures. This limits the choices for the refractory materials for holding Si–Al melts at high temperatures and vacuum conditions. The present research is an endeavor to modify the graphite crucibles for treating the Si–Al melts at high temperatures. This paper presents an insight investigation on the Si and Si–Al melts interaction with graphite crucibles. It outlines a methodology for the graphite passivation by SiC for treating the Si–Al melts at high temperatures in graphite crucibles.

2. Experimental procedure

In this research, Silgrain™ with 99.7% purity and high purity Al (99.99%) were used as the initial materials. The melting process was carried out in a high-density graphite crucible. The physical and chemical properties of the graphite can be found in Table 1. In order to investigate the interaction of Si melt with the graphite crucible at long times, Si was melted in the crucible and held at 1500 °C and 1800 °C for 1 h. Subsequently, the cross section of graphite crucible was investigated by the Scanning electron microscopy (FESEM, Zeiss Ultra 55) and the phases were characterized by Energy dispersive spectroscopy technique (EDS). In addition, the interaction of Si melt with graphite at short time was studied by dipping a piece of graphite (the same graphite grade as the crucible) to the Si melt and holding it for only 5 min at 1500 °C. The surface and cross-section of this sample was also investigated by SEM. The interaction of Si–Al melt with graphite crucible was also investigated by doping 80 g of Al into 320 g of Si melt at 1500 °C. In order to prepare the Si–Al alloy, a piece of pure Al rod (80 g) was hung on a 20 cm of a graphite thread, which was attached on a Molybdenum (Mo) handle. The Mo handle was installed on the furnace chamber and could be slide down and up. As the Si was melted in the graphite crucible, the Al sample was dipped into the melt at 1500 °C. The Al dissolved in Si in some seconds and the remained graphite thread was pulled out of the melt. This mechanism was also applied for dipping the graphite sample immersed in the Si melt and holding it for 5 min. The experiments f Si-graphite interaction took place in Ar atmosphere of a purity degree of 99.999%. The interaction of Si-20 wt%Al with graphite was investigated

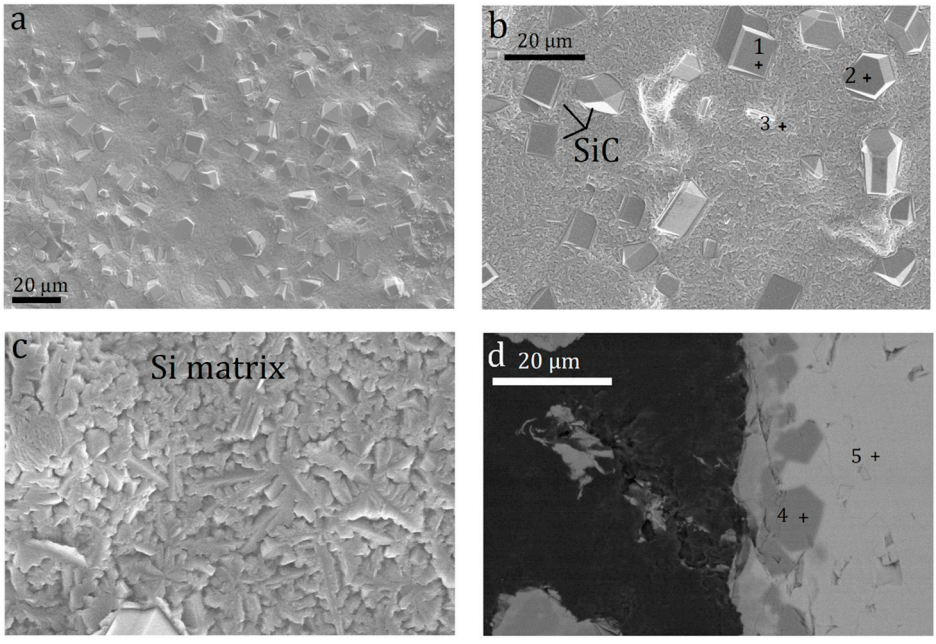

Fig. 1. SEM micrographs of the graphite sample submerged into Si melt at 1500 °C and held for 5 min, (a–c): vertical view to the surface of the graphite sample (d,e): the cross-section of the submerged sample representing the interface of graphite-Si.

Table 2
Chemical compositions of the spots on the SEM images characterized by EDS.

Figure	EDS Spot no.	Chemical composition (at%)		
		C	Si	Al
Fig. (1a)	1	59.82	40.18	_
Fig. (1b)	2	53.67	46.33	_
Fig. (1b)	3	4.64	95.36	_
Fig. (1e)	4	50.64	49.36	_
Fig. (1e)	5	0	100	_
Fig. 7	6	52.17	47.83	_
Fig. 8	7	31.06	56.44	12.51
Fig. 8	8	22.4	1.43	76.17
Fig. 8	9	54.71	45.28	_
Fig. 8	10	6.75	92.46	0.78
Fig. (13b)	11	0.37	0.81	90.83
Fig. (13c)	12	36.43	57.41	6.16
Fig. (16b)	13	48.23	51.77	_
Fig. (16b)	14	47.9	52.1	_

in vacuum conditions and it was carried out over the pressure range of 1–10 Pa. A schematic sketch of the furnace's chamber applied in this research can be found in Ref. [21]. The chamber was vacuumed to 1 Pa and purged by Argon three times before running the experiment to make sure there is not any air left in the chamber. X-ray diffraction (XRD, Bruker - Da Vinci) method was employed to investigate the phases formed in the graphite crucible due to the melt infiltration. During the vacuum treatment of the Si–Al melt, several samples were taken from the melt were and characterized by ICP-MS to determine the melt composition as a function of vacuum treatment time.

3. Results and discussion

3.1. Interaction of Si melt with graphite

Previous researches in the literature showed a thin layer of silicon carbide (SiC) forms at the graphite surface in contact with silicon [22–24]. Here we dive into the formation mechanism of SiC layer on graphite surface by investigating the surface of the graphite sample immersed in liquid silicon, which is shown by images a-c in Fig (1). The cross-section of the immersed sample is also shown in Fig (1d). Various spots of the SEM images presented in Fig (1) are characterized by EDS and the composition of each spot is presented in Table (2). Looking at Figs (1a, b) some crystals can be seen forming in hexagonal and tetragonal shapes on the surface of the graphite sample. The matrix is also shown at higher magnification in Fig (1c). The EDS characterizations of the spots marked on Figs (1 a-c) reveal that the crystals growing from the graphite surface are SiC, while surrounded by a Si layer. This silicon layer on the graphite surface is actually the solidified liquid silicon on the graphite surface Fig (1c). This Si layer, sticking on the graphite, is expected as liquid silicon wets graphite in which the wetting angle is very low and can be 0–28° depending to surface roughness [23]. Therefore, when the immersed graphite sample is pulled out from the melt, a thin film of silicon is remained on surface and so has not detached from the graphite. Fig. (1d) represents the cross-section of Si and graphite after 5 min and it indicates that the SiC nuclei are loosely attached to the graphite interface. The interaction of Si melt with graphite crucible at longer times are shown in Fig (2). This figure presents the cross-section of the crucible's wall, corner, and bottom in contact with Si melt after 1 h of interaction at 1500 °C. As Fig (2 a-c) shows, a continuous layer of SiC is developed on the graphite surface after 1 h. The higher magnifications of the SiC layer presented in Fig (2d) also reveals that the SiC surface layer formed on the graphite at 1500 °C is consisted of SiC grains with an average diameter of 15 (±5) μm that are joined to the graphite substrate directly with the grain boundaries upright to the graphite body. Considering Fig (1) and Fig (2), it can be concluded that SiC crystals are formed on the surface of graphite at the initial minutes of melting process and by continuing the process they grow to get closer to each other and make a continuous layer of SiC on the graphite surface. The cross-section of graphite and Si melt after treating at 1800 °C for 1 h is represented in Fig (3). Comparing Figs (2) and (3), it can be concluded that the SiC layer is disintegrated at high temperatures and there are many SiC grains attached to the crucible only by one side seeming to be detached from crucible and close to be released to the melt. The higher magnifications of the SiC layer show the surface of graphite is covered with a thin multi crystalline SiC layer consisted of small SiC grains with average size between 2 and 4 μm. Fig. (3c) shows those SiC grains that are still attached to the crucible are connected to the graphite surface directly and there are not any small grains under the marked crystals. This can be better seen in Figs (3d and e) where the stacking faults of SiC grains are clearly visible. Fig. (3d and e) indicate that the SiC grain boundries are weak for keeping the big SiC

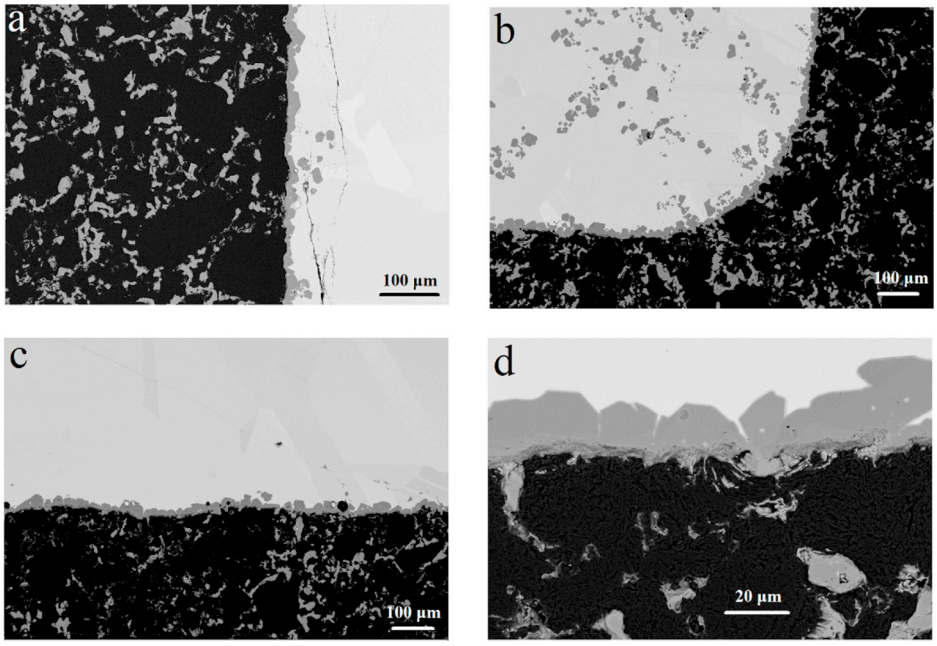

Fig. 2. SEM micrographs (QBSD images) of the graphite crucible after holding Si melt at 1500 °C for 1 h.

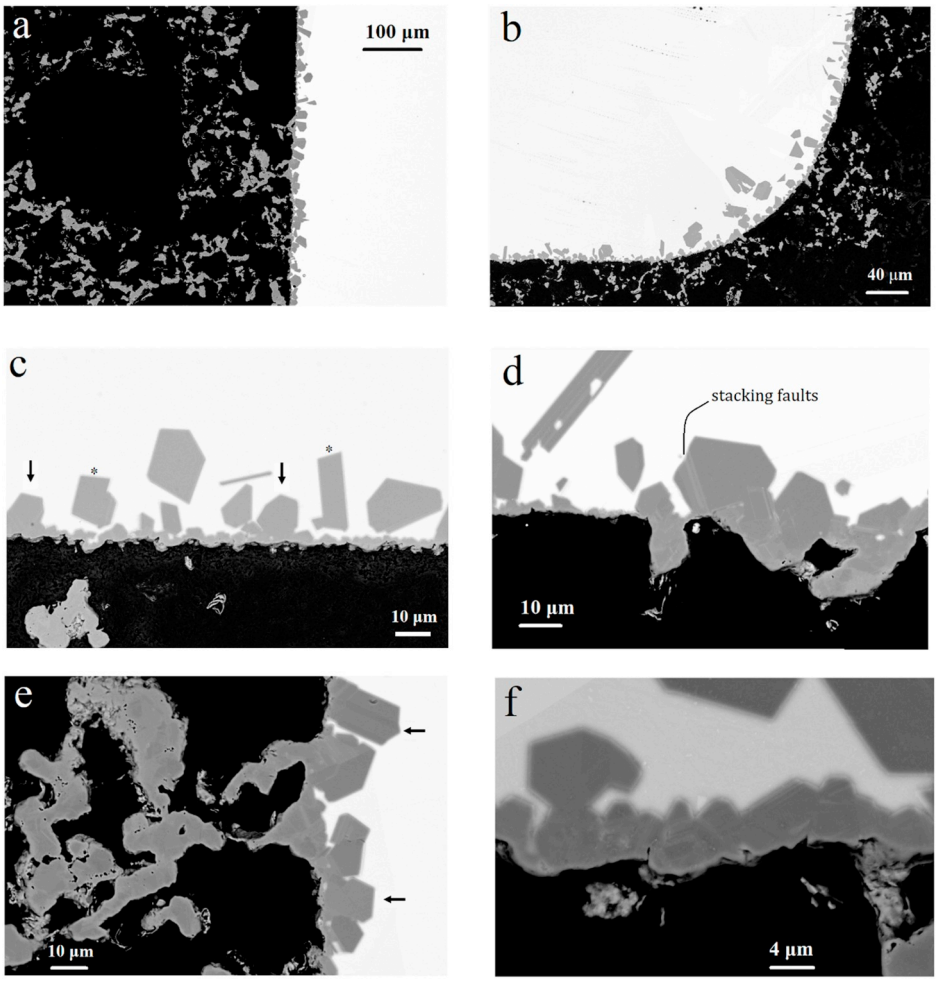

Fig. 3. SEM micrographs (QBSD images) of the graphite crucible after holding Si melt at 1800 °C for 1 h.

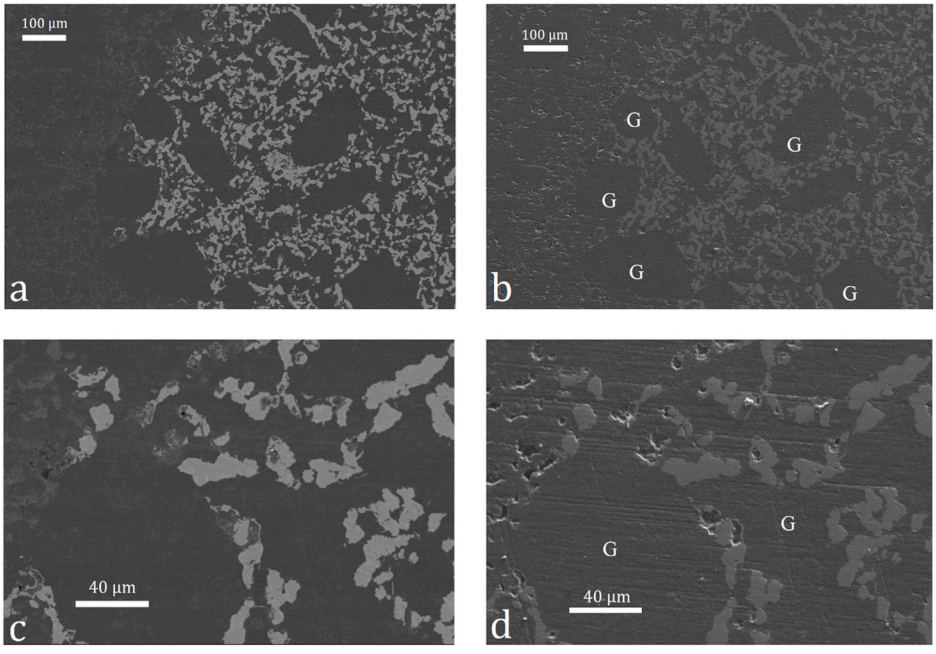

Fig. 4. The infiltrated region of the graphite crucible after 1 h of holding Si melt at 1500 °C.

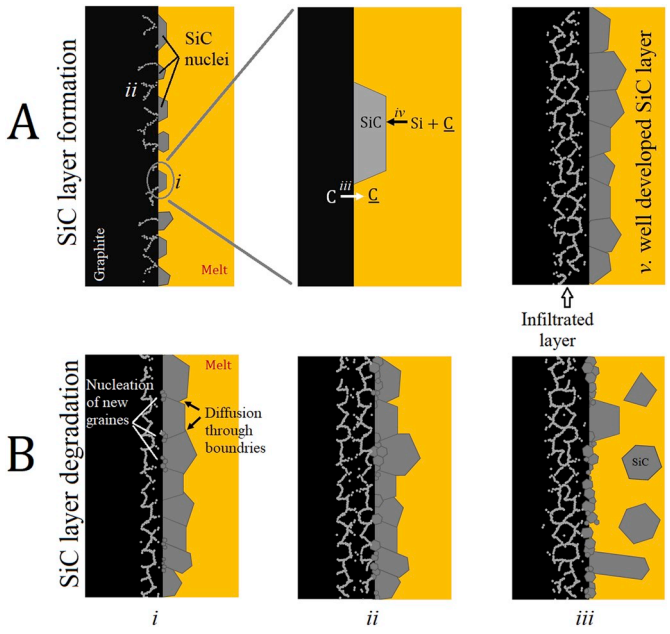

Fig. 5. The schematic illustration of the Si melt-graphite interaction showing the mechanism of SiC formation and growth.

grains connected to the cruible body. It should be mentioned that by increasing the temperaute, the diffusion through the grain bounries of SiC layer are increased, making it possible for the Si to diffuse through the boundries and reach the graphite surface. Subsequently the primary SiC grains can be seperated from the graphite body as new grains are nucleating at the graphite surface. Then the new grains can grow up and the same phenomenon can happen for them. This process can take place over and over and each time a SiC grain will be replaced by several grains leading to the surface layer to become thiner and with more grain boundries. Thus, it can be concluded that the SiC layer is more intigrated and thicker at low temperature, while the layer that is formed at higher temperatures not only has a thinner thickness but also it has a greater density of grain boundaries.

In addition to the surface SiC layer, an infiltrated layer consisted of SiC particles has formed in the graphite body as it is seen in Figs (2 and 3). The melt infiltration front in the graphite crucible is shown in Fig (4). Looking at these images, it can be concluded that melt infiltrates to the graphite body through the porosity network by filling the pores one by one if the graphite surface is not covered by the growing SiC. The pores are between the graphite grains that are marked as "G" on Figs (4 b, c). Therefore, the pores would get locked as the SiC is formed in the pores of the graphite body, which, subsequently stops the infiltration of further melt into the graphite body. Regarding the information we obtained from Figs (1-4), now we can explain the interaction mechanism of graphite with Si melt. Fig. (5A) is presenting various steps of Si melt interaction with graphite schematically. Each step on this figure is also explained as follows;

i. Nucleation of SiC crystals on the graphite surface.
ii. Melt infiltration to the graphite body through the porosity parallel to *i*.
iii. Dissolution of solid C into Si melt at graphite-melt interface.
iv. Growth of SiC crystals at the graphite surface by the reaction of Si and dissolved carbon, and formation of SiC in the pores of the graphite body.
v. Radial growth of SiC crystals to get close to each other leading to block the surface by making a fully developed SiC layer.

Finally, by developing of the layer of SiC at the surface and formation

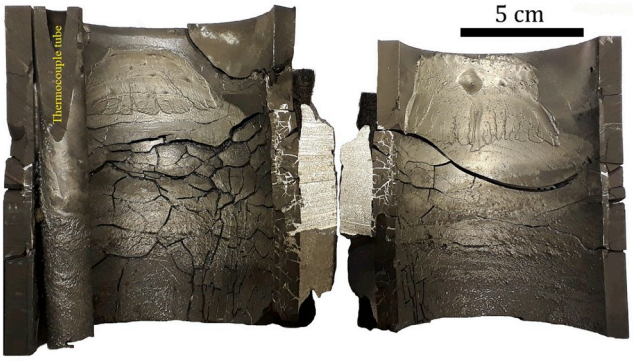

Fig. 6. The photograph of the graphite crucible after adding Al to Si at 1500 °C. The crucible burst immediately after the allying process.

SiC in the pores of the graphite body, the melt infiltration into the graphite body is stopped. When the SiC layer is fully developed, the dissolution of carbon into the melt, which causes the SiC layer thickening, is however continued with a very low rate as it needs diffusion of carbon through the SiC boundaries. The degradation mechanism of the SiC layer, which takes place mainly at high temperatures due to the faster diffusion through grain boundaries, is also presented in Fig (5B) and explained as follows:

i. Diffusion of Si through the primary SiC grain boundaries toward the graphite interface.
ii. Formation and growth of the new grains at the graphite-SiC interface.
iii. Detaching of the primary SiC grains.

In addition, it should be mentioned that at higher temperatures the SiC nucleation and growth has a faster kinetics and the melt has a higher stirring velocity in induction furnace. This can also accelerate the detaching of the SiC grains from the graphite surface. The discussions presented in this section showed the SiC layer formed at 1500 °C temperature was more integrated and had a lower density of grain boundaries compared to the layer formed at 1800 °C, and hence will act better as a passive layer.

3.2. *Interaction of Si–Al melt with graphite*

As mentioned before, for the investigations on the Si–Al interacting with graphite crucible, Si was melted in the crucible and subsequently Al was immersed to the melt. After a few minutes of alloying the Si with Al, the crucible burst and melt drained away completely. The same experiment was repeated two times more and the same phenomenon was observed. Fig. (6) shows the photos of the two halves of a graphite crucible, which is burst after doping by Al. In order to unveil the mechanism of the crucible degradation, the cross section of the crucible was inspected by SEM. Fig. (7) represents the SEM micrographs of the graphite-metal cross section. Obviously, a thin layer of SiC is on the interface of the graphite-melt, and an infiltration region is formed inside the graphite crucible due to the melt infiltration. Fig. (7a) shows the infiltrated layer itself is consisted of two layers; a dark layer and a bright layer, which are called as the 1st and 2nd layers, respectively, in this paper. The 2nd layer (deeper in graphite) is shown at higher magnifications in Fig (7b and c). These figures show the bright layer is consisted of multi-phase particles and would be discussed in detail later. The 1st layer is also depicted at higher magnifications in Fig (7d). The phases formed in this layer were characterized by EDS and it was confirmed that they are SiC (EDS spot 6 in Table 2). The surface layer formed on the graphite surface is also shown in Fig (7e) in which the surface layer formed on the graphite is composed of two phases that are characterized

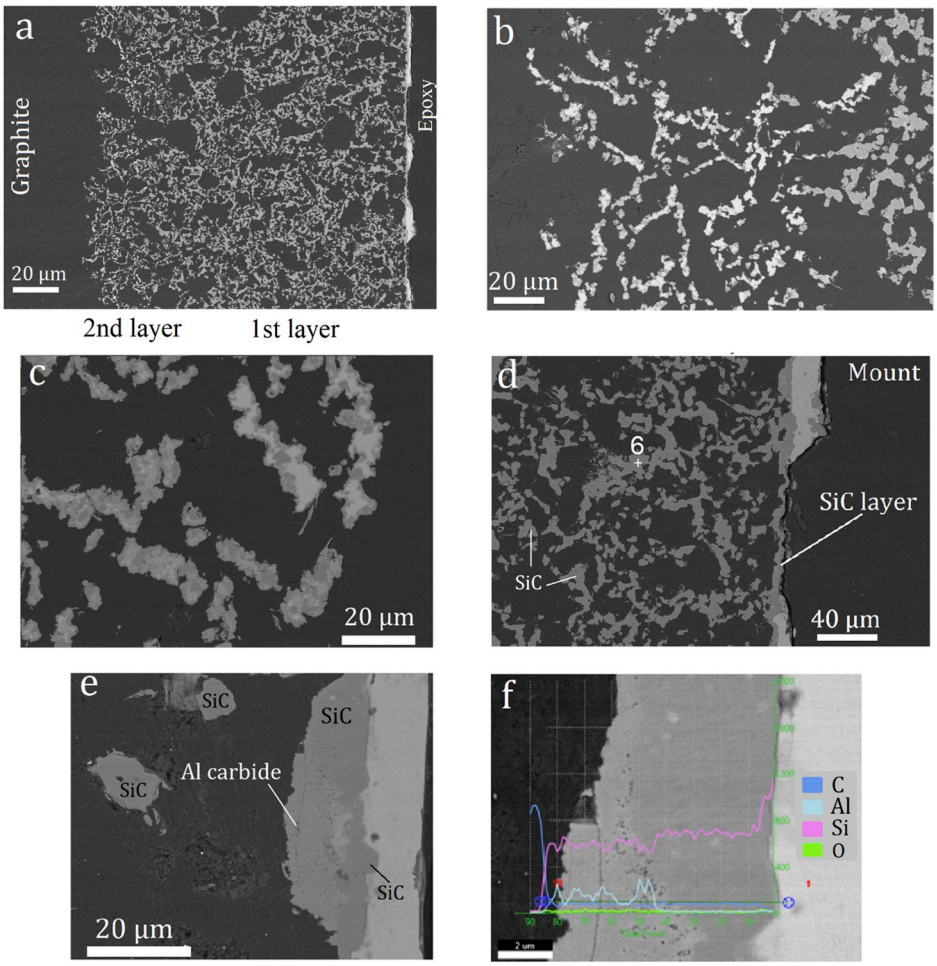

Fig. 7. SEM-BS micrographs belonging to the burst graphite crucible after adding Al to Si melt at 1500 °C, (a): cross-section of the graphite crucible representing the two infiltrated layers formed in the graphite, (b, c) 2nd infiltrated layer at higher magnifications. (d): the 1st layer at higher magnifications, (e): the surface layer formed on the graphite crucible, (f): The EDS line scan of the surface layer.

by EDS line scanning in Fig. (7f). This figure shows that the dark phase that has a rigid structure is only consisted of Si and C. However, the bright phase which has a porous structure is consisted of Al, Si, and C. The 2nd diffused layer and their corresponding EDS maps are presented in Fig (8). This figure shows the same porous structure is formed in the 2nd diffused layer as well. The EDS maps makes it clear that the dark hexagonal phases are consisted of Si and they are free of Al, while the porous phases are consisted of Al. The EDS spot characterization of the porous phase (EDS spots 7 and 8) is presented in Table 2, indicating that the porous structures are composed of Al and C. However, there is about 56.4% Si in spot 7, the spot 8 is almost free of Si (1.4%) and has a chemical composition close to aluminum carbide (Al_4C_3). Formation of Al_4C_3 in the system of Si–Al–C has also already reported in Refs. [25–27]. In addition, EDS characterizations of the spots 9 and 10 in Fig (8) show that the dark phases with hexagonal shapes are SiC and the bright phases are unreacted Si with C. Thus, it can be concluded that the second layer is consisted of Si, SiC, and Al_4C_3. Hence the 1st product layer is formed during the melting process where the graphite was in contact with molten Si and the 2nd layer is formed immediately after doping Al into Si melt. As discussed in section 3.1, it takes time for the SiC layer to grow completely on the graphite surface and passivation occurs. However, as shown in Fig (1 a-d), when Si is alloyed with Al there are still lots of areas on the graphite surface without the continuous SiC layer formed on it. This makes it possible for the Si–Al melt to infiltrate to the graphite body which causes the 2nd layer. The formation of the carbides can be represented by the following reactions:

$$Si + C = SiC, \quad \Delta G_{1500\ ^\circ C} = -54250\ J \tag{1}$$

$$4Al + 3C = Al_4C_3, \quad \Delta G_{1500\ ^\circ C} = -97500\ J \tag{2}$$

$$Si + 4Al + 4C = Al_4SiC_4, \quad \Delta G_{1500\ ^\circ C} = -160900\ J \tag{3}$$

Reactions (1–3) all possess negative values of Gibbs energy indicating that all carbide phases at 1500 °C, are feasible to form. However, in the case of Si–Al alloy the activity of the elements is a function of the melt composition, thus the Gibbs energy of the above reactions would change by melt composition as well. One can calculate the Gibbs formation energy for the Al and Si carbides from Si–Al melts by considering the partial molar Gibbs energy of mixing for Al and Si as presented in the following reactions calculated by FactSage® software (FTlite database) [28]:

$$Si = \underline{Si}, \quad \Delta G_{(4)} = \overline{G}^{M}_{Si} = R.T.\ln(a_{\underline{Si}}) \tag{4}$$

$$Al = \underline{Al}, \quad \Delta G_{(5)} = \overline{G}^{M}_{Al} = R.T.\ln(a_{\underline{Al}}) \tag{5}$$

Where the underlined $\underline{Si}$ and $\underline{Al}$ in the above reactions indicate the Si and Al are in the solution state, $\overline{G}^{M}_{Si}$ and $\overline{G}^{M}_{Al}$ show the partial molar Gibbs energy of mixing as a function of molar fraction of Al (x_{Al}) in the melt, respectively. The $a_{\underline{Si}}$ and $a_{\underline{Al}}$ denote the activity of $\underline{Si}$ and $\underline{Al}$ in the and can be expressed thorough the following equations at 1500 °C (FactSage® software):

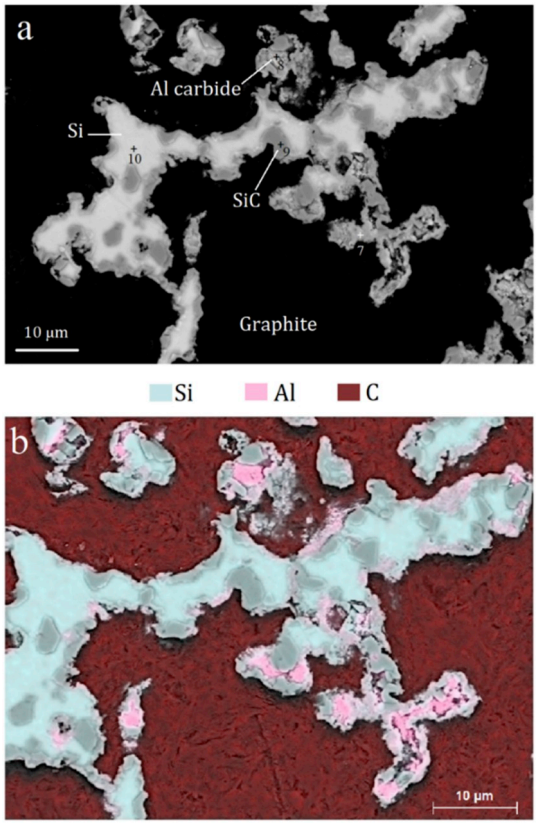

Fig. 8. (a): The SEM-BS micrograph showing the phases formed in the graphite body at the 2nd layer. (b): the corresponding EDS maps.

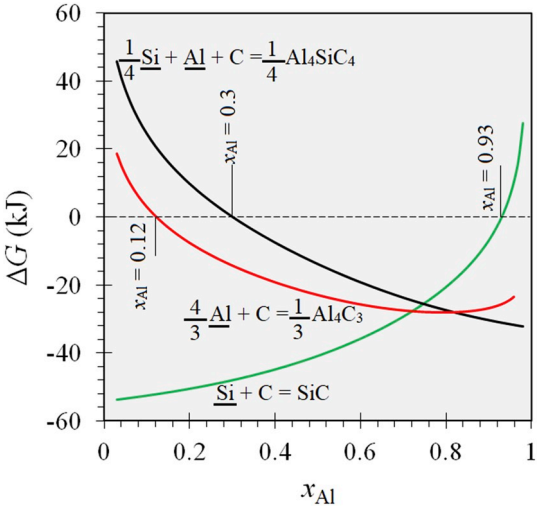

Fig. 9. Gibbs free energy of formation for the SiC, Al_4SiC_4, and Al_4C_3 from 1 mol of C and as a function of x_{Al}.

$$a_{\underline{Si},\ 1500\,^{\circ}C} = -0.8595x_{Si}^3 + 1.6198x_{Si}^2 + 0.2367\,x_{Si} + 0.0093 \quad (6)$$

$$a_{\underline{Al},\ 1500\,^{\circ}C} = -1.0409x_{Al}^4 + 1.4584x_{Al}^3 + 0.1183x_{Al}^2 + 0.462x_{Al} \quad (7)$$

Now by applying Hess's law on the reactions (1–5) and by considering the solution state for the dissolved species, carbide formation reactions from Si–Al melts can be rewritten as follows:

$$\underline{Si} + C = SiC,\quad \Delta G_{(8)} = \Delta G_{(1)} - \Delta G_{(4)} = -54250 - RT.\ln(a_{\underline{Si}}),\ J \quad (8)$$

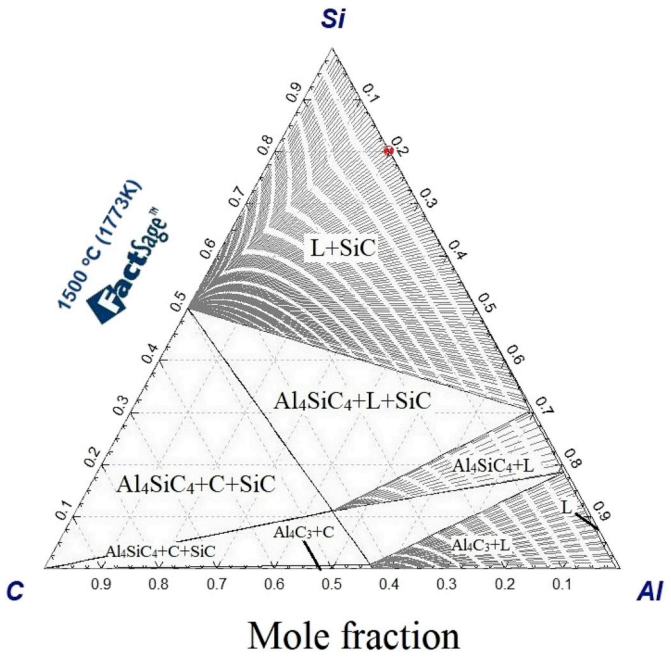

Fig. 10. The ternary phase diagram of Si–Al–C at 1500 °C.

$$\frac{4}{3}\underline{Al} + C = \frac{1}{3}Al_4C_3,\quad \Delta G_{(9)} = \frac{1}{3}\Delta G_{(2)} - \frac{4}{3}\Delta G_{(5)} = -32500 - \frac{4}{3}RT.\ln(a_{\underline{Al}}),\ J \quad (9)$$

$$\frac{1}{4}\underline{Si} + \underline{Al} + C = \frac{1}{4}Al_4SiC_4,\quad \Delta G_{(8)} = \frac{1}{4}\Delta G_{(3)} - \frac{1}{4}\Delta G_{(4)} - \Delta G_{(5)} = -40225 - RT.\ln\left(a_{\underline{Al}}.a_{\underline{Si}}^{\frac{1}{4}}\right),\ J \quad (10)$$

Considering the activity definition for element i in the melt as $a_i = x_i.\gamma_i$, the change in Gibbs formation energy for SiC, Al_4C_3, and Al_4SiC_4 through reactions (8–10) and as a function of (x_{Al}) can be calculated as presented in Fig (9). Reactions (8–10) are balanced for consumption of 1 mol carbon and thus the carbides can be compared with regard to their stability, similar to the Ellingham diagrams. Thus, the curves that are at lower positions in Fig (9) show the more favorable reaction. This figure indicates that for low concentrations of Al in the melt ($x_{Al} < 0.12$) the only stable carbide is SiC, but by increasing the x_{Al} the Al_4SiC_4 and Al_4C_3 become stable at $x_{Al} = 0.12$ and 0.3, respectively. However, in real conditions, as the Si–Al melt infiltrates to the graphite body, various ratios of Si–Al–C could be experienced in local positions hence the Si–Al–C phase diagram should be applied here to study the formation of feasible phases. The Si–Al–C ternary phase diagram at 1500 °C is presented in Fig (10) as calculated by FactSage® thermodynamic software and the initial composition of the Si-20 wt%Al melt is marked on the diagram. As the melt infiltrates to the graphite body the local composition shifts toward the bottom side and left vertex of the triangle where the SiC, Al_4C_3, Al_4SiC_4, and C are the stable phases.

3.3. Structural stress due to carbide formation

As we showed in section 3.2, the failure of the crucible corresponds to the formation of Al carbides in the graphite body. The formation of carbide species in the graphite body exerts considerable stresses in the material leading to the degradation of the crucible. Table (3) presents the volume change and the distortion exerted on the crucible due to the

Table 3
Theoretical volume change and volume strain exerted on the graphite body per 1 mol of carbon.

Reaction	ΔV	ϵ %
Si + C = SiC	7.376	1.39
4/3 Al + C = 1/3 Al_4C_3	15	2.83
Al + C + ¼ Si = ¼ Al_4SiC_4	12.17	2.29

formation of SiC and aluminum carbides through reactions (8–10). The volume change and strain exerted in the crucible can be calculated through the following equations:

$$\Delta V = V_{Carbide} - V_{Graphite} \tag{11}$$

$$\Delta\% = \frac{\Delta V}{V_{Carbon}} \times 100 \tag{12}$$

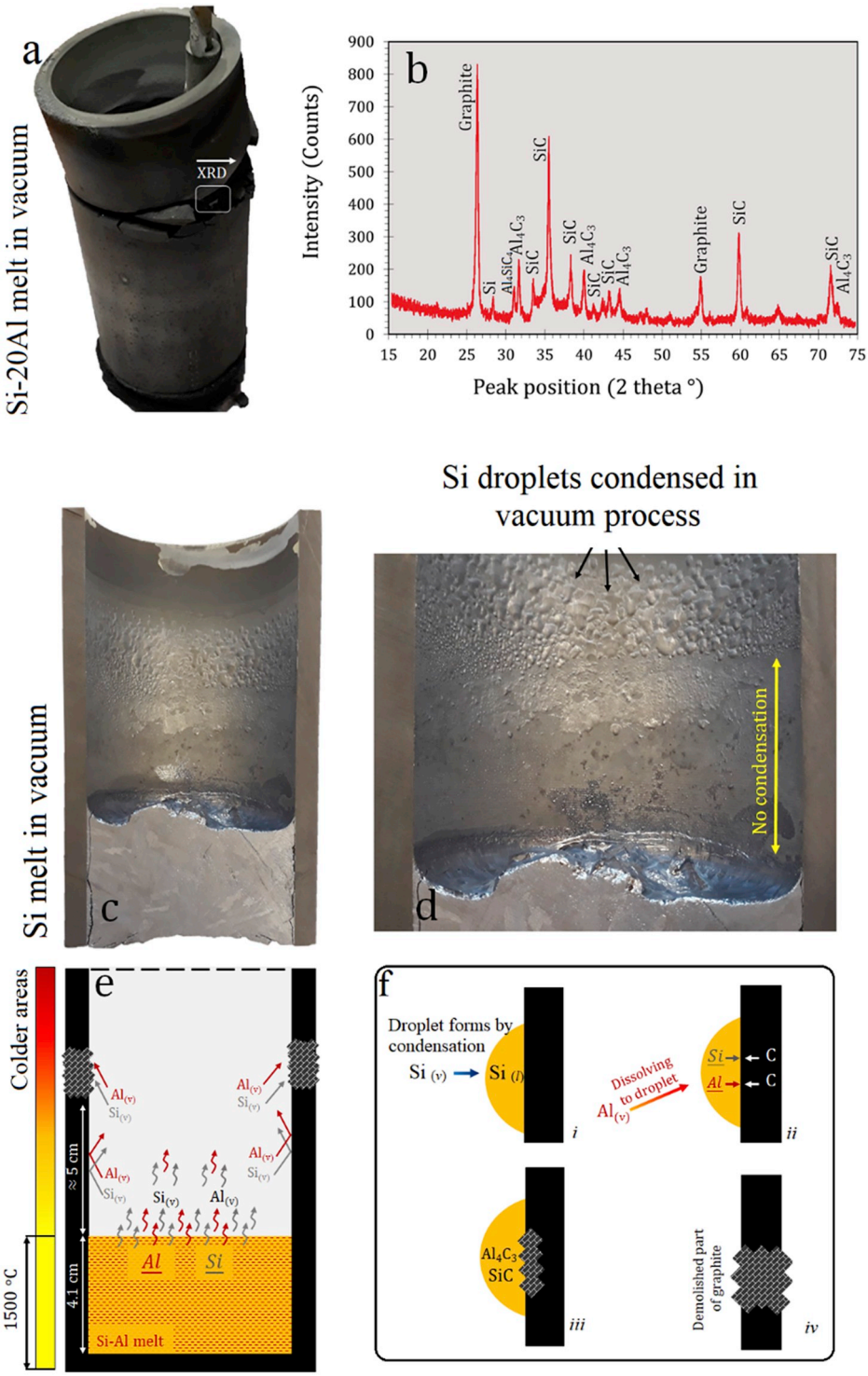

Fig. 11. (a): the photograph of the treated crucible after 1 h of holding Si-20 wt%Al at 1500 °C. (b): XRD pattern of the demolished part of the crucible. (c, d): photographs of the graphite crucible after holding Si at 1500 °C for 1 h. (e): schematic illustration of the evaporation phenomena from the melt, (f): schematic illustration for the mechanism Si–Al fumes interactions with graphite crucible.

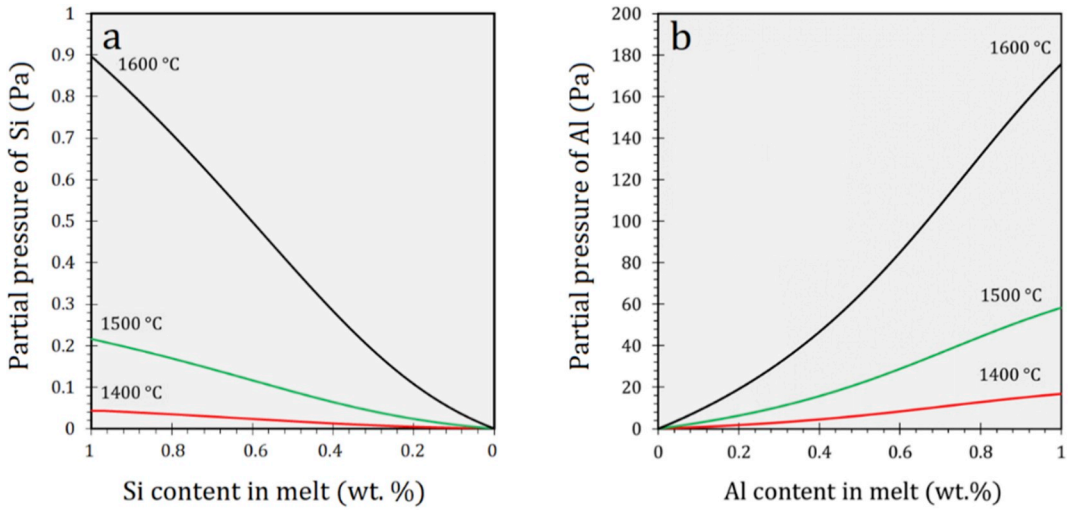

Fig. 12. The partial vapor pressure of Si and Al in the Si–Al system at various temperatures.

where ΔV denotes the volume change for the formation of carbide from 1 mol of carbon. The $V_{Carbide}$ and V_{Carbon} denote the volume of the carbide and graphite per mole of carbon. Table (3) reveals the volumetric strains for the formation of Al_4C_3 and Al_4SiC_4 from 1 mol of carbon are much more than that of SiC. Therefore, Al carbides in the graphite body exerts more strain on the graphite crucible which can be the main cause of the degradation of graphite crucible seen in Fig. (4), which is in a good agreement with results of Jacquier et al. [29]. Table (3) shows the strain exerting from the formation of SiC itself is also considerable, but the results presented in section 3.1 showed that graphite can hold the Si melt for long times without being destructed. This can be related to the fact that the SiC layer which forms on the graphite can passivate the graphite surface and stop the melt infiltration and so the development of SiC formation to a critical level. Our experiences in using graphite crucibles for many years show that more porous graphite has a higher chance for breakage even in the case of holding Si melt, which is due to more SiC formation in the body. However, as Figs (7e and 8) showed, the aluminum carbides have a porous structure and as they form on the surface, they cannot passivate the graphite surface. In addition, the wetting angel of graphite with Al and high Aluminum Si alloys decreases intensively at temperatures higher than 1100 °C [30]. Thus, Al addition to Si melt increases the melt infiltration to the graphite body. Therefore, graphite crucible cannot hold Si–Al alloys at high temperatures.

3.4. Si–Al melt interaction with SiC-passivated crucible

It was experienced that the SiC-passivated crucible, by melting of Si for 1 h at 1500 °C, succeeded later to hold the Si-20 wt%Al alloy without degradation. However, in the vacuum conditions, as it is shown in Fig (11a), after 90 min of holding the Si–Al melt in the crucible, the top part of the crucible (around the neck of the crucible where is not in contact with the melt) was cracked due to the reaction with the condensed phase that evaporated from the melt surface due to lower temperatures on the upper part of crucible. In order to unveil the mechanism of the crucible destruction at the top part we characterized the cracked part of the crucible by XRD and the result is illustrated in Fig (11b). The XRD pattern shows the degraded part of the crucible is consisted of C, SiC, Si, Al_4C_3, and Al_4SiC_4 phases. This indicates on the considerable evaporation of the Si and Al from the melt which further condensed and reacted with the top part of the crucible. Fig. (11c and d) shows the cross-section of a graphite crucible after holding Si melt for 1 h. This figure represents the inner side of a graphite crucible after holding Si melt in vacuum conditions at 1500 °C and before adding Al to the melt. Fig. (11c and d) reveal that there are many droplets formed on the upper crucible wall at the same height as the passivated crucible where Si was alloyed with Al. This shows Si evaporates during the vacuum conditions and condenses at higher levels of the crucible's wall, where the temperature is lower than the Si melting point. Fig. (11e and f) illustrate a schematic of the phenomena taking place in a crucible holding Si–Al during the vacuum conditions. Fig. (11e) shows the Si and Al gas atoms evaporated from the melt hit the crucible's wall and since there is a temperature gradient in the vertical direction, the vapors are condensed at these colder regions on top of the crucible. As Si vapor condenses on the wall, some liquid droplets of $Si_{(l)}$ will form on the crucible wall during the vacuum process. This phenomenon is schematically shown in Fig (11f) where the Al vapor is dissolved into the Si droplets formed on the graphite crucible and start interacting with the graphite body to form Al_4C_3 and destroying the crucible with the same mechanism discussed in section 3.2. The vapor partial pressure of Al and Si (p_{Al} and p_{Si}, respectively) in the Si–Al melts as a function of Al content are calculated as shown in Fig (12). This figure shows that p_{Al} is hundred times higher than p_{Si} in Si–Al melts, making the evaporation of Al to be tremendously higher than Si in vacuum conditions. However, as Si has higher melting point than Al (1410 °C and 660 °C, respectively) the top part of crucible could be a cold place for Si to condense and form the Si droplets on the graphite wall where Al can dissolve in.

The melt composition over time of the vacuum treatment is presented in Table (4). As this table shows, Al content in the melt decreases by the vacuum treating time. Table (4) is in good correspondence with the vapor pressure of Al and Si presented in Fig (12), indicating on the

Table 4
Concentration of Al and P in the Si-20 wt% Al alloy over the time of the vacuum refining at 1500 °C characterized by ICP-MS, the data of this research are compared with P removal from Si melt by vacuum refining reported in Refs. [11,17].

Research and melt composition	Element (wt.%)	Initial content	30 min	60 min	90 min	150 min
This research (Si–20Al melt)	Al	19.95	17.5	12.27	11.39	–
	P	18×10^{-4}	16.44×10^{-4}	11.25×10^{-4}	4.25×10^{-4}	–
Safarian (Si melt) [11,17]	P	16.66×10^{-4}	18×10^{-4}	13.87×10^{-4}	–	9.8×10^{-4}

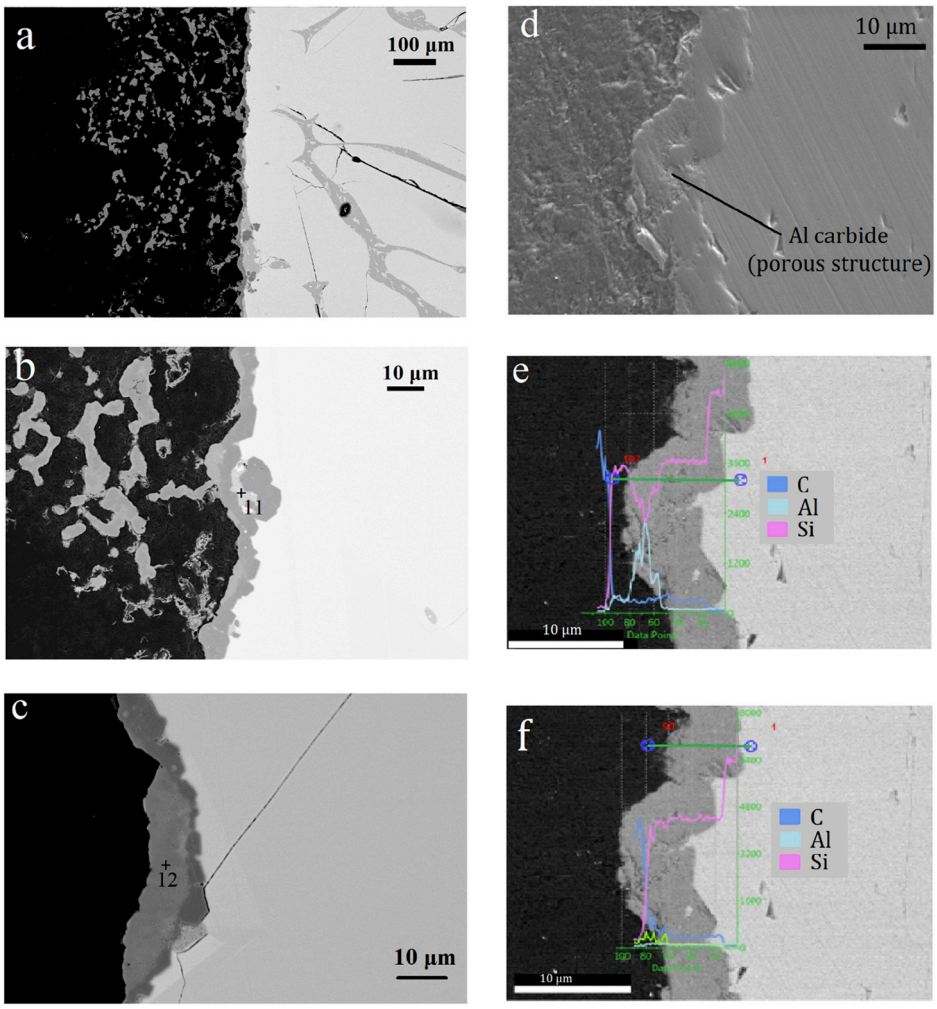

Fig. 13. SEM micrographs of the graphite and Si–Al melt interface. (a–c): infiltrated layer and the primary SiC layer on the surface. (d): the secondary electrons micrograph of the interface. (e, f): the BSE and EDS line scans of two different lines corresponding to the (e).

greater evaporation extent of Al due to its higher vapor pressure. Thus, the vapors emitting from the melt surface in vacuum conditions would mainly consist of Al vapor. In addition, the P concentration in the Si–Al melt over the time of vacuum refining is also included in the Table (4) and is compared with the P removal from Si melt by Safarian in Refs. [11,17]. Table (4), indicates that at 1500 °C the P evaporation from Si-20 wt%Al melt has a faster kinetics compared to Si melt. This indicates that Al addition to the Si accelerates the vacuum evaporation of P from Si, which has high importance for production of SoG-Si.

Although the top part of the SiC-passivated crucible was degraded during the vacuum treatment, the bottom part was found solid and without any crack after holding the Si–Al melt for 1 h. Fig (13) shows SEM micrographs belonging to the cross-section of this crucible. Fig. (13a) shows the infiltrated layer in graphite body is only consisted of SiC particles and Al compounds cannot be detected in the crucible body. This shows that the SiC-passive layer process was successful to prevent the Si–Al melt infiltration to the graphite body. The SiC surface layer is illustrated in Fig (13 b, c) and it shows that the SiC layer covers the graphite surface continually. However, it was barely possible to find some phases rich of Al generated at the surface. The EDS line scans in Fig (13 d-f) compares the rigid and porous parts of the surface layer which indicates that the porous structure is consisted of Al. At this point two scenarios could be considered for Al interaction with the primary SiC layer;

a Reaction of Al in the melt with the primary SiC layer

b Diffusion of Al and/or C through the primary SiC grain boundaries to form Al carbides through the reaction of Al and C.

Which can be expressed through the following reactions:

$$SiC + \frac{4}{3}\underline{Al} = \frac{1}{3}Al_4C_3 + \underline{Si}\ ,\quad \Delta G_{(13)} = \Delta G_{(8)} - \Delta G_{(9)} = 21750 + R.T.\ln\left(\frac{a_{\underline{Si}}}{a_{\underline{Al}}^{\frac{4}{3}}}\right),\ J \tag{13}$$

$$SiC + 4\underline{Al} + 3C = Al_4SiC_4,\ \Delta G_{(14)} = -\Delta G_{(1)} + \Delta G_{(3)} - 4\Delta G_{(5)} = -106650 - RT.\ln\left(a_{\underline{Al}}^4\right),\ J \tag{14}$$

$$SiC + Al_4C_3 = Al_4SiC_4,\quad \Delta G_{1500\,^\circ C} = -11900,\quad J \tag{15}$$

Reaction (13) presents the SiC layer destruction with Al. Reaction (14) presents the SiC interaction with the diffused Al and/or C through the SiC grain boundaries and reaction (15) presents the interaction of primary SiC layer with the possibly formed Al_4C_3 at the surface of SiC by the reaction of diffused C and Al in the melt. Fig. (14) presents the standard Gibbs energy changes for the reactions (13–14) over a wide range of melt composition. As we see, reactions (13) and (14) have a

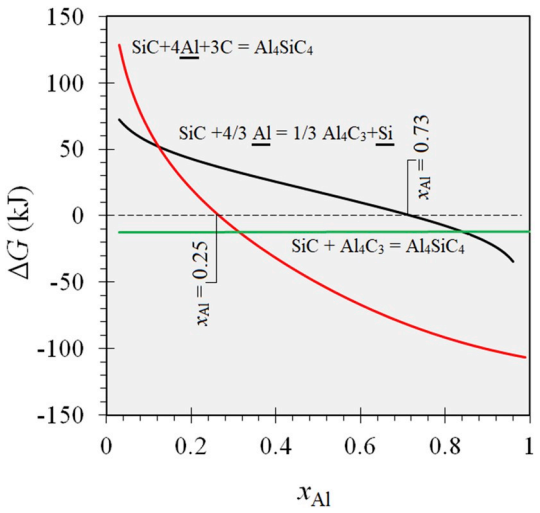

Fig. 14. Gibbs energy change for the reactions of SiC with Al at 1500 °C and as a function of x_{Al}.

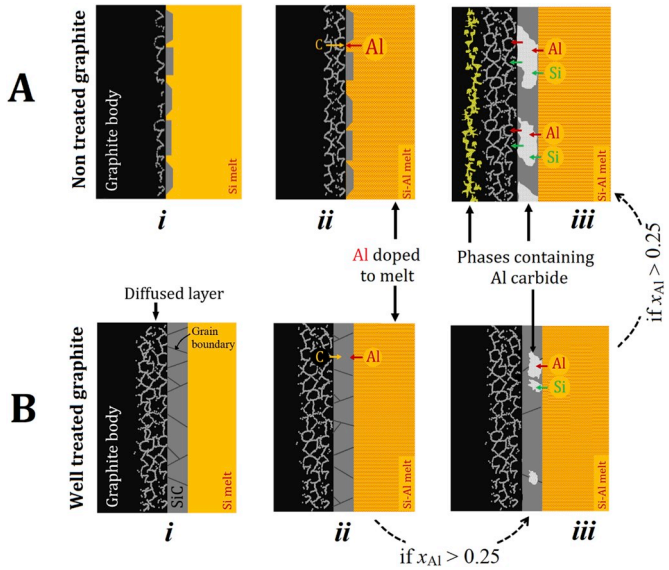

Fig. 15. Schematic illustrations of the melt interaction with graphite crucibles with Si–Al melts. (a): non-treated graphite crucible, (b): SiC passivated crucible before doping Al to the melt.

positive change of Gibbs energy at the Si reach side of Si–Al melt composition and they become negative when if $x_{Al} > 0.73$ and $x_{Al} > 0.25$, respectively, while reaction (15) possess a constant negative Gibbs energy change for all compositions of Si–Al melts. Therefore, for the Si reach alloys of Si–Al melts (where $x_{Al} < 0.25$) in presence of C, reactions (13) cannot take place and the primary SiC layer can tolerate the Si-20 Wt.%Al melt. However, it should also be considered that the local compositions between SiC grains can be different than the melt composition due to Al diffusion. Thus. Reactions (13–15) can take place locally because of high concentrations of Al at some local positions, even at Si–Al melts that are reach of Si. It is worth noting that the development of carbide formation through reaction (13) is depending on the carbon transport in the system and therefore the carbon diffusion (from graphite and through formed SiC) will be a rate limiting and therefore the SiC-passivated layer can stay stable for relatively long times for practical applications.

Fig. (15) compares the proposed mechanisms of Al interactions with the graphite crucible before and after the SiC-passivation process. This figure shows that in the not passivated crucible, the SiC layer is not fully developed when Al is added into Si melt, Fig (15A-i). Thus, most area of the crucible surface is still not passivated by SiC layer and is vulnerable to react with the melt, Fig (15A-ii). Subsequently as Al is added to the melt, Si–Al alloy infiltrates to the graphite body and it forms the Al carbides, Fig (15 A-iii). Regarding the thermodynamic investigations presented in Figs (9 and 10) and the EDS characterizations in Fig (8), the 2nd layer could consist of SiC and Al carbides. However, in the SiC-passivated crucibles, Fig (15B-i), a fully developed SiC passive layer is formed on the graphite surface which prevents the Si–Al melt infiltration to the graphite body. However, if $x_{Al} > 0.25$, carbon can diffuse through the grain boundaries of the primarily SiC layer to react with the Al, Fig (15B-ii). This can lead to the formation of Al carbides and destruction of the SiC layer, Fig (15B-iii).

In order to study if that the SiC degradation by Al can be prevented by excluding the extra C in the system, a SiC crucible was used for melting the Si–Al alloys and holding the alloys for 6 h at 1500 °C and vacuum conditions. Fig. (16) shows the interface of the SiC crucible and the Si–Al alloy after 6 h holding. As can be seen there is no effect of melt interaction with the SiC crucible and its surface is totally free of aluminum carbides. This figure shows that SiC could be an appropriate material for holding Si–Al melts at high temperatures if there is no C in the system. Previous wetting investigations of SiC substrates with Al–Si alloys reach in Al [31] and pure Al [27] showed the formation of Al_4C_3 and the degradation of SiC substrates. These results are in good agreements with the results of Fig (14), where we showed the SiC layer cannot be damaged if it is in contact with Si–Al melts with $x_{Al} < 0.25$, if extra carbon is not present in the system. These results indicate that SiC crucibles are suitable for holding Si–Al melts at high temperatures.

4. Conclusions

The interaction of Si and Si-20 wt%Al melts with graphite and SiC crucibles were investigated at 1500 °C and the main conclusions can be presented as:

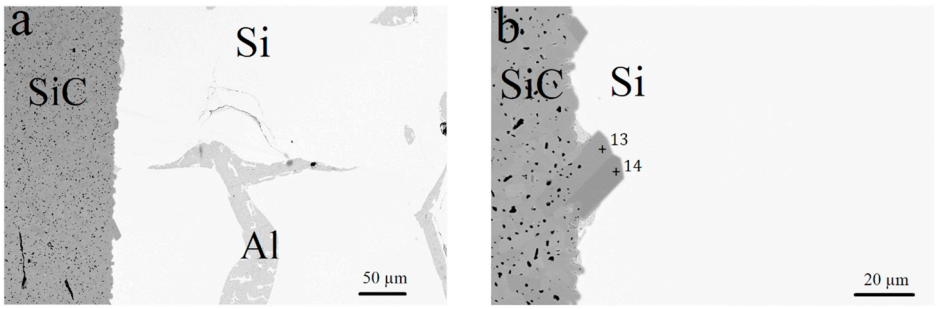

Fig. 16. SEM micrographs of the SiC crucible after holding Si-20 wt%Al melt for 3 h at 1500 °C.

- The SiC layer forming on the graphite crucible is the result of granular growth of SiC nuclei on the graphite surface, which depends on carbon dissolution into silicon and further deposition as SiC.
- It was not possible to hold Si-20 wt%Al melt in the graphite crucible due to melt infiltration to the crucible which led to graphite degradation.
- Aluminum carbides are formed in the graphite body due to the melt infiltration after alloying with Al. A SiC-passivation step for graphite crucible is very helpful to hold the Si–Al melts.
- At vacuum conditions, the not SiC-passivated parts of the graphite crucible may degrade due to the condensation of liquid Si and Al from the gas vapors, and fully passivated surfaces are recommended.
- SiC crucible is stable for Si-20 wt%Al and does not interact with the melt as long as there is no excess of carbon (solid or dissolved in the Si–Al melt).
- Thermodynamics calculations showed the maximum allowed of Al content in in Si–Al alloy for the SiC passivated graphite crucibles and SiC crucibles are 0.25 and 0.73, respectively.

Acknowledgments

This research was financed by Norwegian University of Science and Technology and is done in cooperation with the Research Center for Sustainable Solar Cell Technology (FME SuSolTech) in Norway. The support from Elkem® Bremanger for silicon material is highly acknowledged. The authors express their appreciations to Ivar Andre Ødegård from NTNU for his discussions and comments about the surface passivation of graphite crucibles. The authors appreciate Dr. Yingda Yu from NTNU, for his assistance to provide the QBSD images showing the stacking faults and grain boundaries of the SiC grains by applying the electron channeling technique.

References

[1] Shell Scenarios Shell, Sky - Meeting the Goals of the Paris Agreement, 2018, p. 72. https://www.shell.com/energy-and-innovation/the-energy-future/scenarios/shell-scenario-sky.html.
[2] D.S. Philips, W. Warmuth, Photovoltaics Report, 2016. https://www.ise.fraunhofer.de/de/veroeffentlichungen/studien/photovoltaics-report.html.
[3] J. Safarian, Thermochemical aspects of boron and Phosphorus distribution between silicon and BaO-SiO 2 and CaO-BaO-SiO 2 lags, Silicon 11 (2019) 437–451, https://doi.org/10.1007/s12633-018-9919-8.
[4] T. Jester, Solar-grade silicon: viable option to “EG, Renew. Energy Focus 15 (2014) 34–35, https://doi.org/10.1016/S1755-0084(14)70045-6.
[5] Ceccaroli Forniés, Souto Méndez, Pérez Vázquez, Dieguez Vlasenko, Mass production test of solar cells and modules made of 100% UMG silicon. 20.76% record efficiency, Energies 12 (2019) 1495, https://doi.org/10.3390/en12081495.
[6] A. Datas, A.B. Cristobal, C. del Cañizo, E. Antolín, M. Beaughon, N. Nikolopoulos, A. Nikolopoulos, M. Zeneli, N. Sobczak, W. Polkowski, M. Tangstad, J. Safarian, D. M. Trucchi, A. Bellucci, M. Girolami, R. Marx, D. Bestenlehner, S. Lang, A. Vitulano, G. Sabbatella, A. Martí, AMADEUS: next generation materials and solid state devices for ultra high temperature energy storage and conversion, in: AIP Conf. Proc., 2018, p. 170004, https://doi.org/10.1063/1.5067168.
[7] M.H. Leipold, T.P. O’Donnell, M.A. Hagan, Materials of construction for silicon crystal growth, J. Cryst. Growth 50 (1980) 366–377, https://doi.org/10.1016/0022-0248(80)90260-2.
[8] A. Casado, J. Torralba, S. Milenkovic, Wettability and infiltration of liquid silicon on graphite substrates, Metals 9 (2019) 300, https://doi.org/10.3390/met9030300.
[9] J.K. Lee, J.S. Lee, B.Y. Jang, J.S. Kim, Y.S. Ahn, G.H. Kang, H.E. Song, M.G. Kang, C.H. Cho, 6′ crystalline silicon solar cell with electron-beam melting-based metallurgical route, Sol. Energy 115 (2015) 322–328, https://doi.org/10.1016/j.solener.2015.02.027.
[10] Y. Tan, S. Ren, S. Shi, S. Wen, D. Jiang, W. Dong, M. Ji, S. Sun, Removal of aluminum and calcium in multicrystalline silicon by vacuum induction melting and directional solidification, Vacuum 99 (2014) 272–276, https://doi.org/10.1016/j.vacuum.2013.06.015.
[11] J. Safarian, M. Tangstad, Vacuum refining of molten silicon, Metall. Mater. Trans. B 43 (2012) 1427–1445, https://doi.org/10.1007/s11663-012-9728-1.
[12] J. Jiao, B. Grorud, C. Sindland, J. Safarian, K. Tang, K. Sellevoll, M. Tangstad, The use of eutectic Fe-Si-B alloy as a phase change material in thermal energy storage systems, Materials 12 (2019) 2312, https://doi.org/10.3390/ma12142312.
[13] R. Israel, R. Voytovych, P. Protsenko, B. Drevet, D. Camel, N. Eustathopoulos, Capillary interactions between molten silicon and porous graphite, J. Mater. Sci. 45 (2010) 2210–2217, https://doi.org/10.1007/s10853-009-3889-6.
[14] H. Dalaker, M. Tangstad, Time and temperature dependence of the solubility of carbon in liquid silicon equilibrated with silicon carbide and its dependence on boron levels, Mater. Trans. 50 (2009) 1152–1156, https://doi.org/10.2320/matertrans.M2009034.
[15] H. Dalaker, M. Tangstad, The interactions of carbon and nitrogen in liquid silicon, High Temp. Mater. Process. 33 (2014) 363–368, https://doi.org/10.1515/htmp-2013-0043.
[16] W. Polkowski, N. Sobczak, M. Tangstad, J. Safarian, Silicon and silicon-boron alloys as phase change materials in thermal energy storage units, Silicon Chem. Sol. India (2018), https://doi.org/10.5281/zenodo.1289792.
[17] J. Safarian, M. Tangstad, Kinetics and mechanism of Phosphorus removal from silicon in vacuum induction refining, High Temp. Mater. Process. 31 (2012) 73–81, https://doi.org/10.1515/htmp.2011.143.
[18] S. Hiwasa, Y. Kato, K. Hanazawa, N. Yuge, EvaporationofPhosphorus inMoltenSilicon with electron beam IrradiationMethod, J. Jpn. Inst. Metals 67 (2003) 569–574.
[19] M. Miyake, T. Hiramatsu, M. Maeda, Removal of Phosphorus and antimony in silicon by electron beam melting at low vacuum, Japan Inst. Met. 70 (2006) 43–46.
[20] A. Hoseinpur, J. Safarian, Phosphorus removal from Al-doped silicon by vacuum refining, in: 35th Eur. Photovolt. Sol. Energy Conf. Exhib. Phosphorus, Bruxel, 2018, pp. 469–472, https://doi.org/10.4229/35thEUPVSEC20182018.
[21] J. Safarian, K. Tang, K. Hildal, G. Tranell, Boron removal from silicon by humidified gases, Metall. Mater. Trans. A E. 1 (2014) 41–47, https://doi.org/10.1007/s40553-014-0007-8.
[22] S.L. Shikunov, V.N. Kurlov, SiC-based composite materials obtained by siliconizing carbon matrices, Tech. Phys. 62 (2017) 1869–1876, https://doi.org/10.1134/s1063784217120222.
[23] A. Ciftja, T.A. Engh, M. Tangstad, Wetting properties of molten silicon with graphite materials, Metall. Mater. Trans. A Phys. Metall. Mater. Sci. 41 (2010) 3183–3195, https://doi.org/10.1007/s11661-010-0362-8.
[24] N. Eustathopoulos, Wetting by liquid metals—application in materials processing: the contribution of the grenoble group, Metals 5 (2015) 350–370, https://doi.org/10.3390/met5010350.
[25] X. Han, Y. Huang, S. Zhou, X. Sun, X. Peng, X. Chen, Effects of graphene content on thermal and mechanical properties of chromium-coated graphite flakes/Si/Al composites, J. Mater. Sci. Mater. Electron. 29 (2018) 4179–4189, https://doi.org/10.1007/s10854-017-8363-7.
[26] C. Jacquier, D. Chaussende, G. Ferro, J.C. Viala, F. Cauwet, Y. Monteil, Study of the interaction between graphite and Al-Si melts for the growth of crystalline silicon carbide, J. Mater. Sci. 37 (2002) 3299–3306, https://doi.org/10.1023/A:1016147420272.
[27] P. Shen, Y. Wang, L. Ren, S. Li, Y. Liu, Q. Jiang, Influence of SiC surface polarity on the wettability and reactivity in an Al/SiC system, Appl. Surf. Sci. 355 (2015) 930–938, https://doi.org/10.1016/j.apsusc.2015.07.164.
[28] Factsage software version 7.3, (n.d.). www.factsage.com.
[29] C. Jacquier, D. Chaussende, G. Ferro, J.C. Viala, F. Cauwet, Y. Monteil, Study of the interaction between graphite and Al-Si melts for the growth of crystalline silicon carbide, J. Mater. Sci. 37 (2002) 3299–3306, https://doi.org/10.1023/A:1016147420272.
[30] E. Pastukhov, V. Chentsov, A. Kiselev, Wetting of graphite surface by the aluminium alloys melts, in: Ariel.Ac.Il, 2006, pp. 178–181. http://www.ariel.ac.il/sites/conf/MMT/MMT-2006/Service_files/papers/Session_1/1-178_WE.pdf.
[31] X.S. Cong, P. Shen, Y. Wang, Q. Jiang, Wetting of polycrystalline SiC by molten Al and Al-Si alloys, Appl. Surf. Sci. 317 (2014) 140–146, https://doi.org/10.1016/j.apsusc.2014.08.055.